PNAS

Supporting Information for
Chelation-directed interface engineering of in-place self-cleaning membranes

Xiaobin Yang,[1] Yangxue Li,[1] Dan Wu,[2] Linlin Yan,[3] Jingzhu Guan,[1] Yajie Wen,[1] Yongping Bai,[1] Bhekie B Mamba,[4] Seth B. Darling,[5,6,7]* Lu Shao[1]*

1. MIIT Key Laboratory of Critical Materials Technology for New Energy Conversion and Storage, State Key Laboratory of Urban Water Resource and Environment, School of Chemistry and Chemical Engineering, Harbin Institute of Technology, Harbin 150001, PR China.
2. Longjiang Environmental Protection Group CO., LTD, Harbin 150050, PR China.
3. School of Marine Science and Technology, State Key Laboratory of Urban Water Resource and Environment (SKLUWRE), Harbin Institute of Technology, Weihai 264209, PR China.
4. Institute for Nanotechnology and Water Sustainability, College of Engineering, Science and Technology, University of South Africa, Florida Science Campus, 1709 Roodepoort, South Africa.
5. Chemical Sciences and Engineering Division and Center for Molecular Engineering, Argonne National Laboratory, Lemont, IL 60439, USA
6. Advanced Materials for Energy-Water Systems Energy Frontier Research Center (AMEWS EFRC), Argonne National Laboratory, Lemont, IL 60439, USA
7. Pritzker School of Molecular Engineering, University of Chicago, Chicago, IL 60637, USA

*Corresponding authors, email: shaolu@hit.edu.cn (L. Shao), darling@anl.gov (S.B. Darling)

This PDF file includes:

Figs. S1 to S22

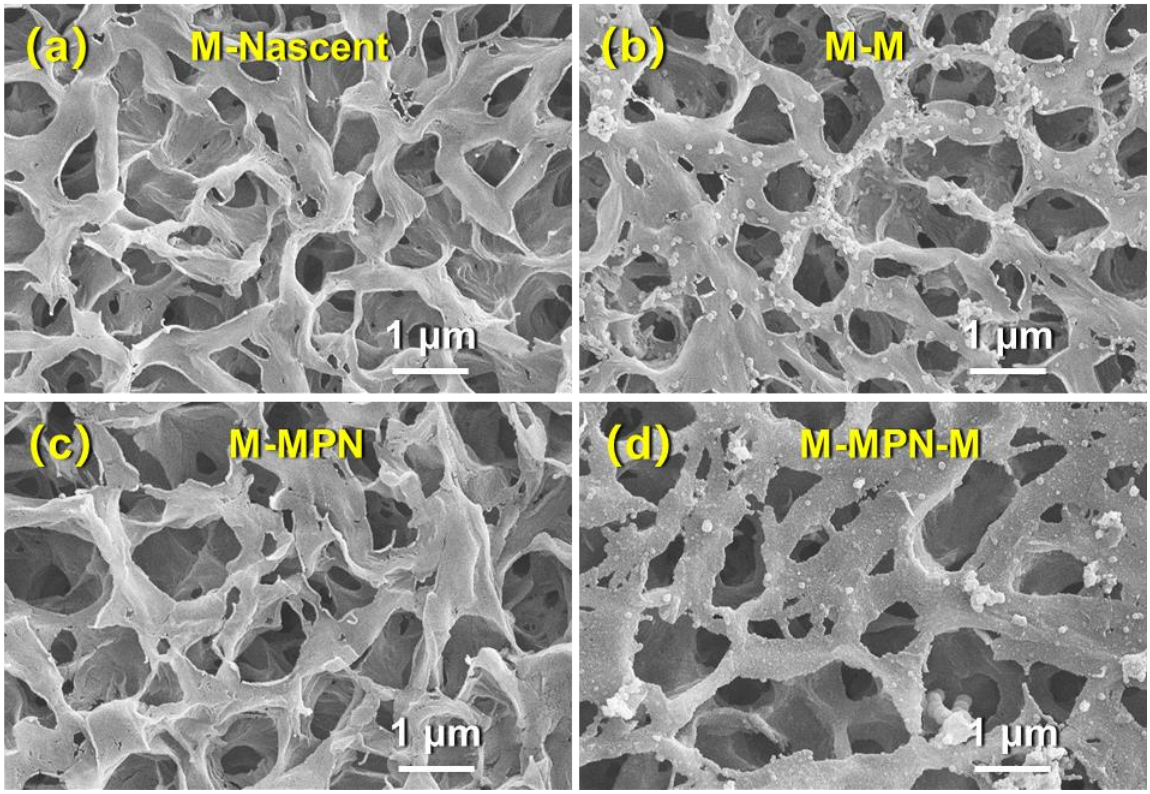

Fig. S1. SEM image of as-prepared membranes with low magnification.

As shown in **Fig. S1**, M-MPN exhibited a negligible change in morphology compared to M-Nascent (material surfaces are smooth), indicating a uniform coating of MPN. Unitary incubation of the Mn^{2+} precursor for M-M resulted in sparse and scattered particles. In contrast, the mineralized membrane M-MPN-M arose dense nanoparticles.

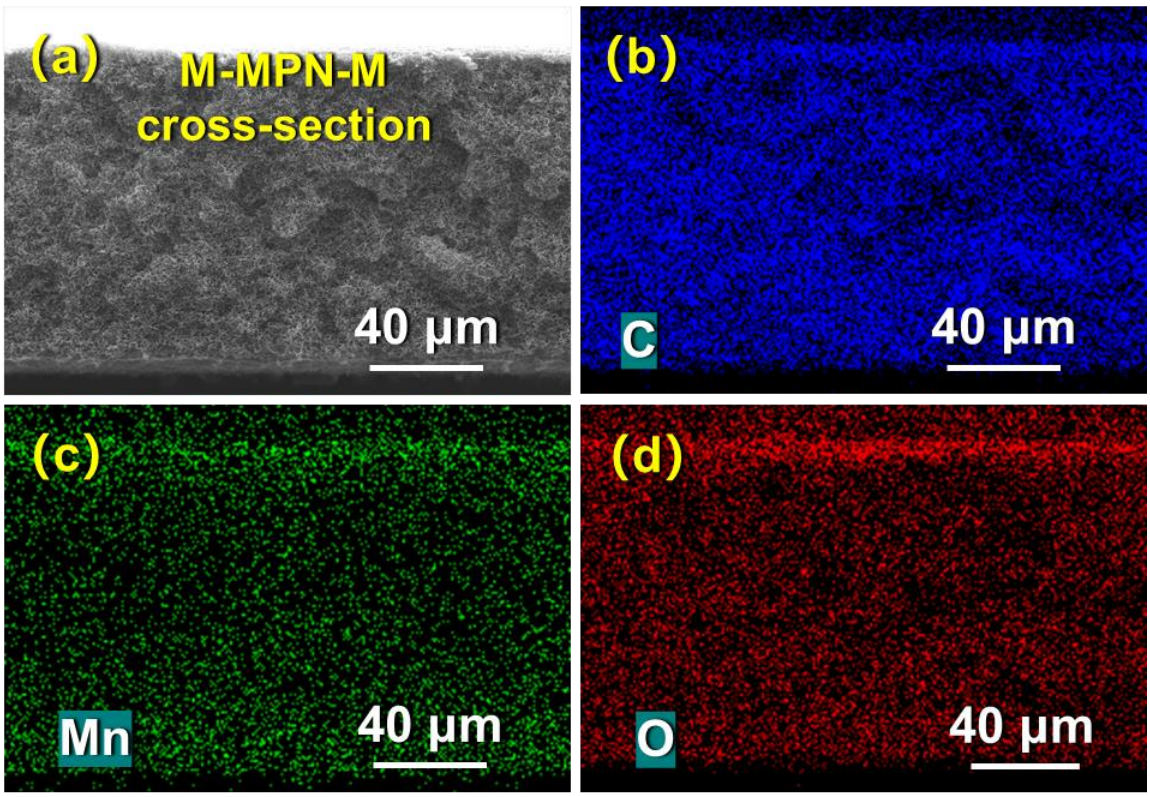

Fig. S2. (a) Cross-section SEM image of M-MPN-M and EDS mapping images of the elements (b) C, (c) Mn, and (d) O.

As shown in **Fig. S2**, EDS mapping was performed on the cross-section of M-MPN-M to measure the element distribution. The representative atoms (C, Mn, and O) exhibit a uniform distribution, indicating that the nano-mineral film at the membrane interface is conformal and uniform.

MnO_2 mineralization in aqueous buffer (pH=8.5):

Fig. S3. Reaction equation of MnO_2 mineralization.

As shown in **Fig. S3**, the mineral precursor of $MnSO_4$ could realize MnO_2 mineralization in an alkaline aqueous buffer by virtue of the dissolved oxygen. The mild and controllable mineralization was realized by the mediation of MPN.

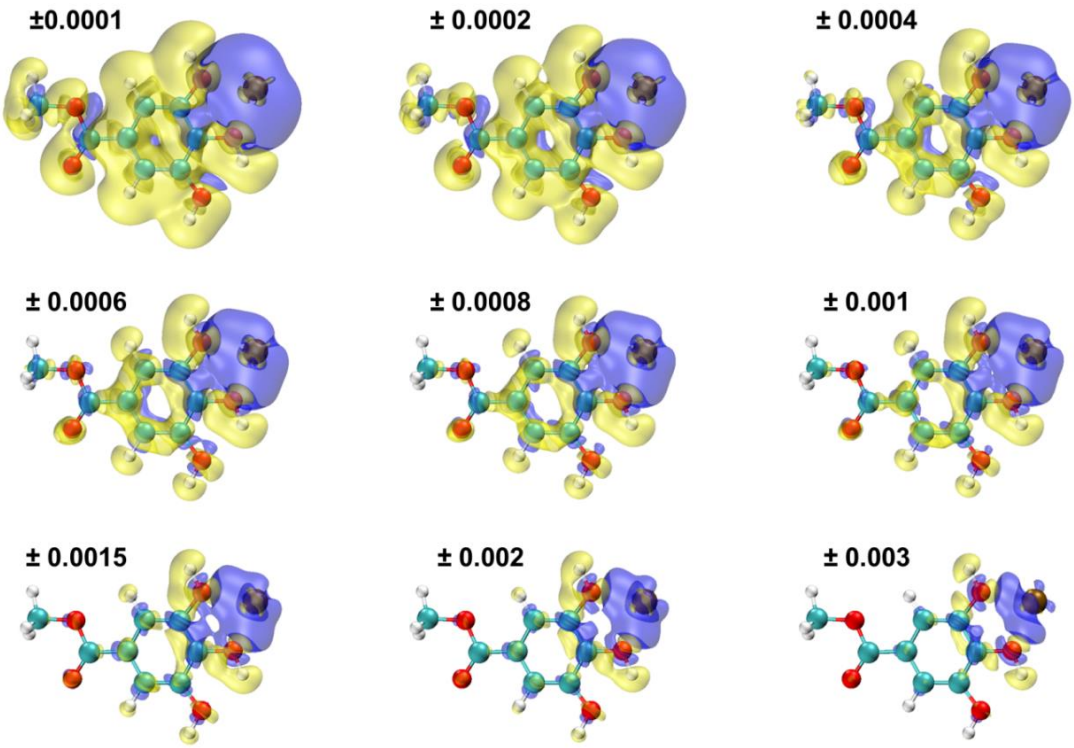

Fig. S4. Multifunctional wavefunction analysis of the optimized equilibrium state. The 3D isosurface map of the electron density difference originating from the interaction of Mn^{2+} and TA via the phenolic hydroxyl groups. The blue and yellow surfaces in the 3D isosurface maps represent positive and negative isovalues (marked with specific isovalues), respectively.

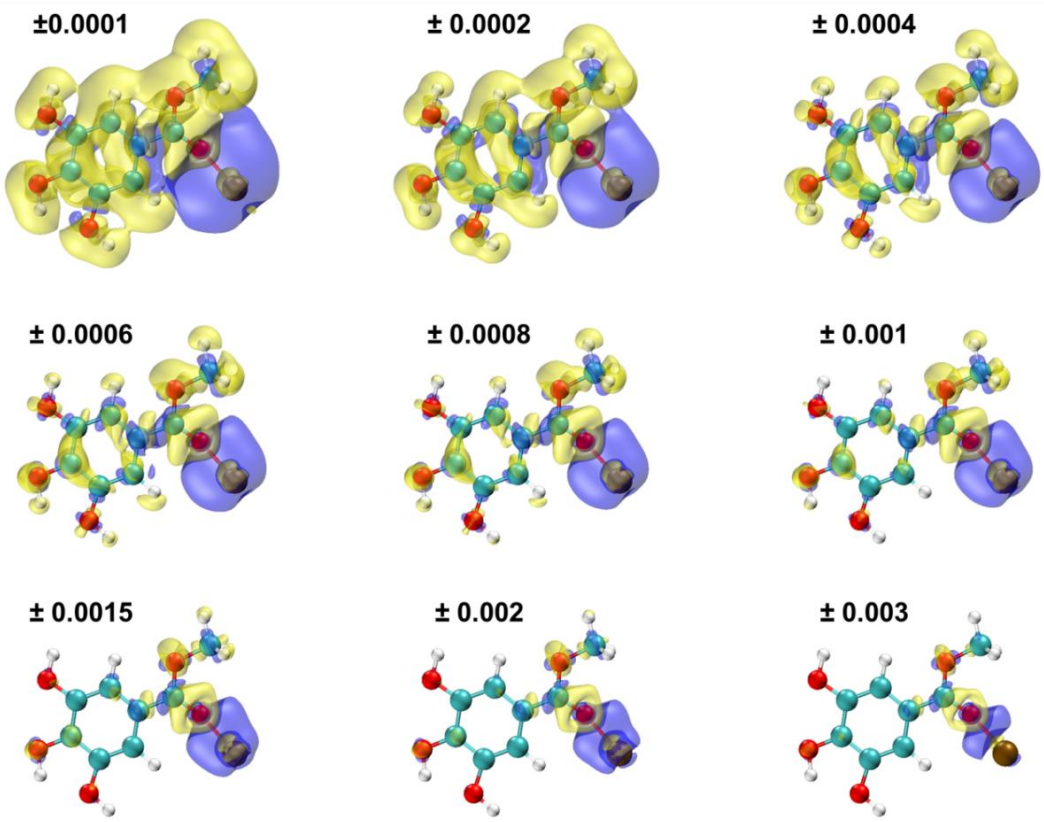

Fig. S5. Multifunctional wavefunction analysis of the optimized equilibrium state. The 3D isosurface map of the electron density difference originating from the interaction of Mn^{2+} and TA via the ester group. The blue and yellow surfaces in the 3D isosurface maps represent positive and negative isovalues (marked with specific isovalues), respectively.

As shown in **Figs. S4** and **S5**, the gallate-Mn interactions resulted in similar blue electron-rich bell-like structures hanging the yellow electron-deficient Mn cores irrespective of the values of the 3D isosurfaces.

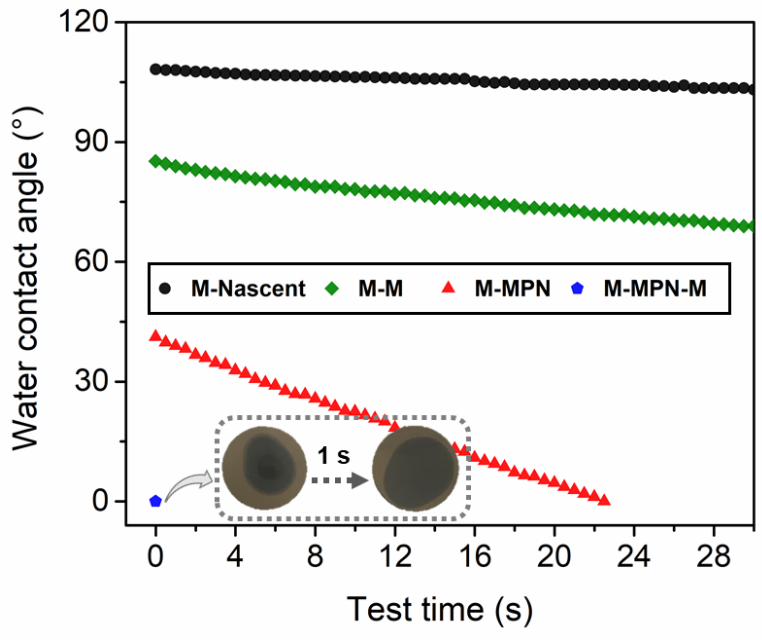

Fig. S6. Dynamic water contact angles of as-prepared membranes.

To detail the hydrophilization through the membrane cross-section, dynamic WCAs were also recorded (**Fig. S6**). The real-time WCAs of M-MPN and M-M exhibit a gradual decrease, indicating a certain hydrophilization outwork. The M-MPN-M could be quickly wetted by the water droplet and allowed to penetrate through the membrane after sucking it inside (inset).

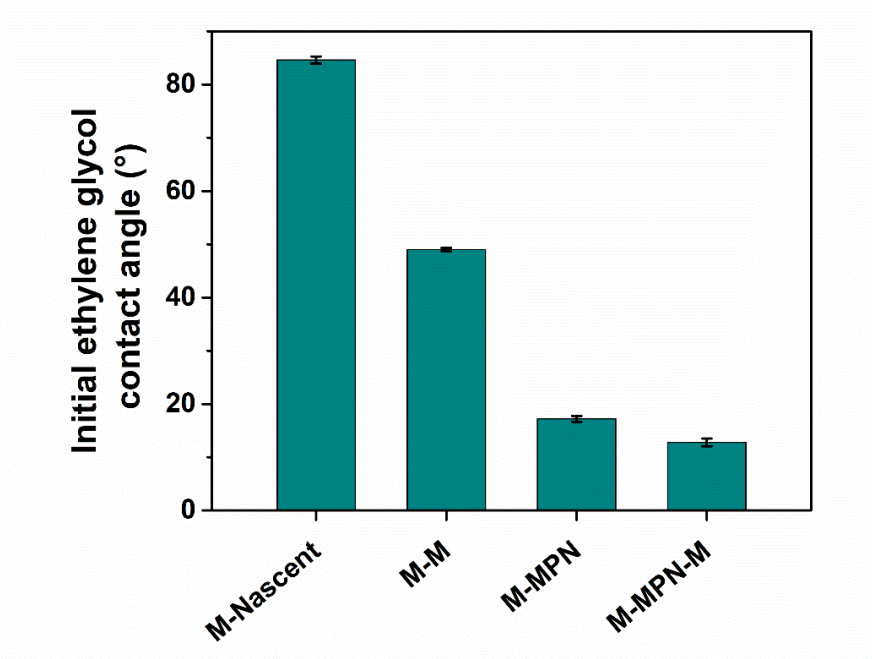

Fig. S7. Initial ethylene glycol contact angles of the membranes.

The apparent surface energy of one membrane is crucial for evaluating its hydration capacity. It is typically determined as a sum of the dispersive and polar components of the membrane and can be statistically calculated using the water and ethylene glycol contact angles **(Fig. S7**) according to **Equations 1** and **2**:

$$\gamma_l(1+cos\theta) = 2\left(\gamma_l^p\gamma_m^p\right)^{1/2} + 2\left(\gamma_l^d\gamma_m^d\right)^{1/2} \quad (1)$$

$$\gamma_m = \gamma_m^d + \gamma_m^p \quad (2)$$

where *γ* represents the apparent surface energy, the subscripts *l* and *m* stand for immersion liquid and membrane, and the superscripts *d* and *p* stand for dispersive and polar components, respectively. *θ* refers to the corresponding contact angles.

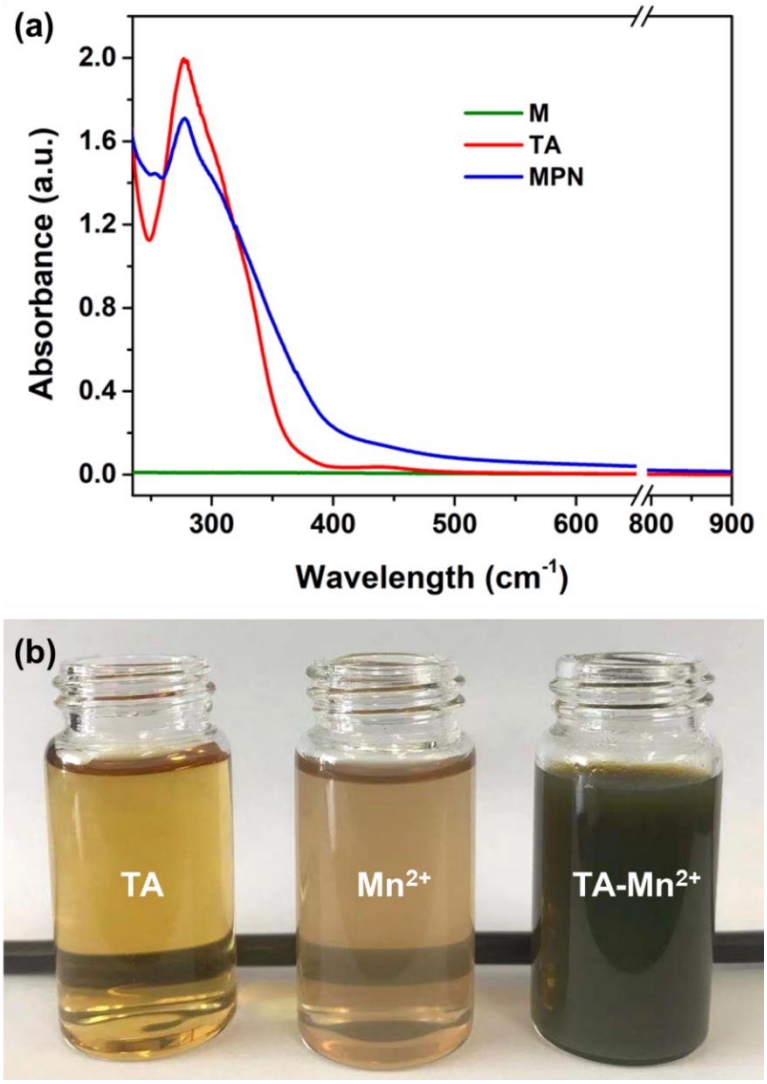

Fig. S8. (a) UV-Vis spectra and (b) digital photos of the one-hour incubated aqueous solutions.

From the UV-vis spectra (**Fig. S8a**), there arose a new peak in the region of 400~600 cm^{-1}, which was attributed to the coordination of phenol groups and Mn^{2+}. This indicates the formation of a metal-polyphenol network (MPN). Meanwhile, after 1 h of incubation (**Fig. S8b**), obvious precipitation occurred in the incubated aqueous solutions containing TA and Mn^{2+}, indicating the strong inner interactions of the MPN.

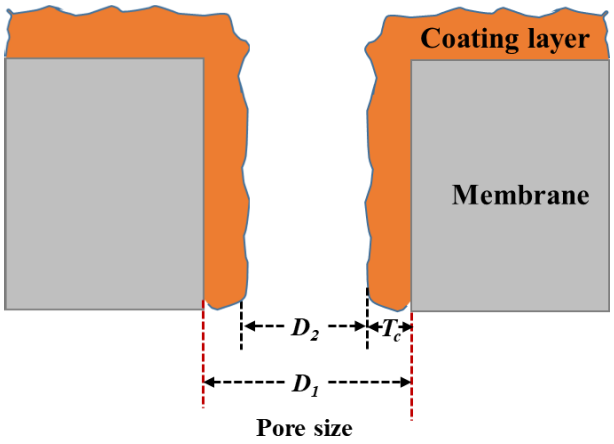

Fig. S9. Schematic illustration of evaluation of the thickness of the coating layer by pore size before and after coating.

As shown in **Fig. S9**, the thickness of the coating layer (T_c) is the change of half of the pore diameter ($0.5\times(D_2-D_1)$).

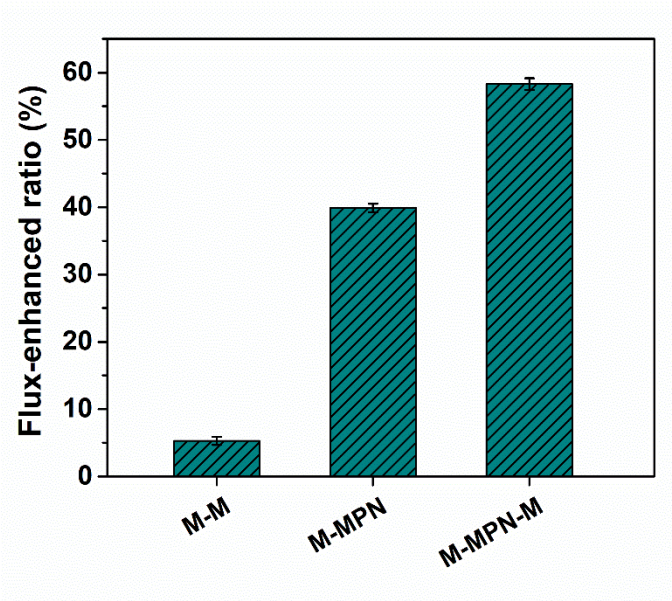

Fig. S10. Water permeance increment ratio of as-prepared membranes relative to M-Nascent.

Fig. S10 shows the water permeance increment ratio of the as-prepared membranes relative to that of M-Nascent. M-MPN-M exhibits a 58.3% increase in water permeance compared to M-Nascent.

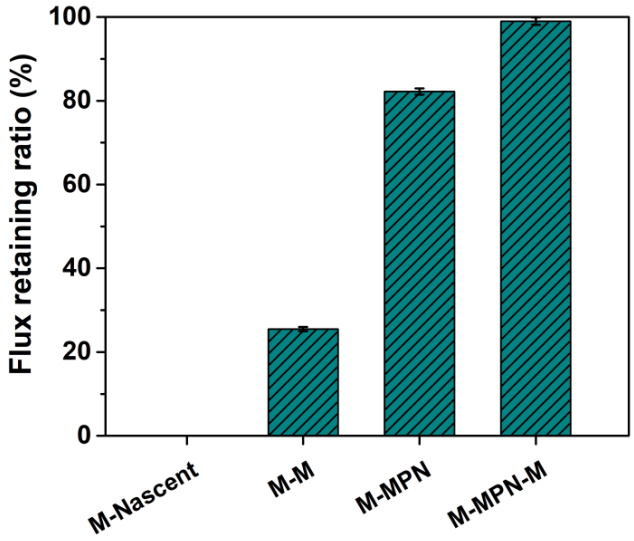

Fig. S11. Water permeance retaining ratio of the dry membrane relative to the wet membrane.

As shown in **Fig. S11**, the water permeances of dry membranes were contrasted to reveal the hydration capability difference and potential for dry-state storage; M-MPN-M has the highest permeance-retaining ratio of 99.0% relative to the wet membrane.

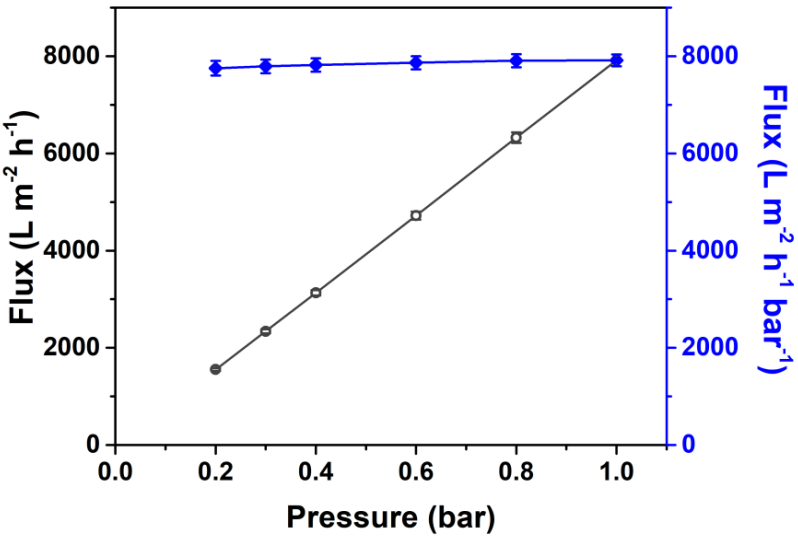

Fig. S12. Water permeance of the M-MPN-M under various transmembrane pressures.

As shown in **Fig. S12**, the pressure-flux relationship was investigated for M-MPN-M. As a result, it exhibits relatively consistent pressure-normalized permeance when adopting transmembrane pressures of 0.2, 0.3, 0.4, 0.6, 0.8, and 1.0 bar.

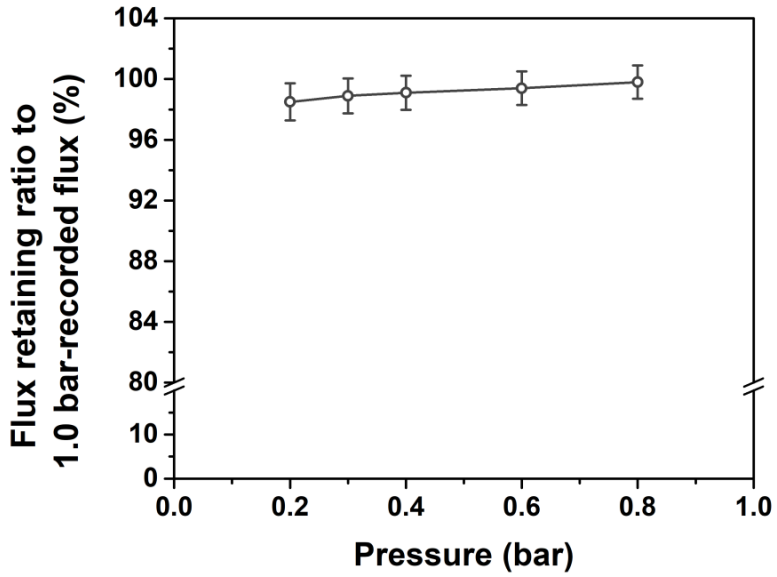

Fig. S13. Water permeance retaining ratio of M-MPN-M to 1.0 bar-recorded permeance when adopting transmembrane pressure of 0.2, 0.3, 0.4, 0.6, and 0.8 bar.

As shown in **Fig. S13**, water permeances under 0.2~0.8 bar retain over 98% relative to the 1.0 bar-recorded permeance. Water permeance under 0.3 bar retains 98.9% of that under 1.0 bar. Then, we used a low operating pressure of 0.3 bar for ease of operation.

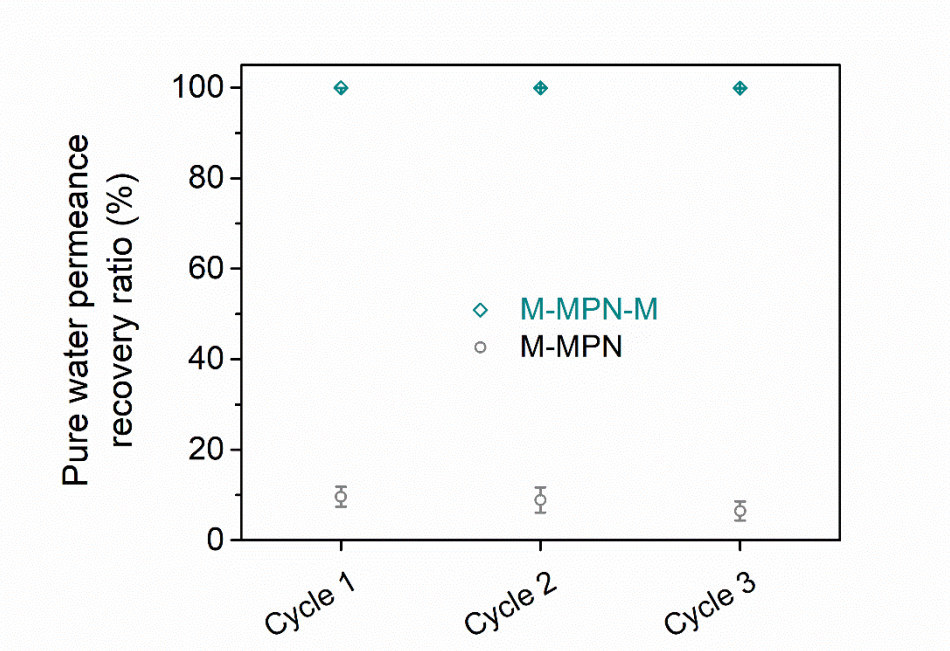

Fig. S14. Pure water permeance recovery ratios after *n*-cycle regeneration during repeated crude oil-in-water emulsion separations.

As shown in **Fig. S14**, the mineralized membrane M-MPN-M could be almost regenerated with pure water permeance by in-place H_2O_2 cleaning. In stark contrast, M-MPN could not be regenerated with the same cleaning treatment. The above results verified the significant catalytic regeneration capability of the as-prepared ultrathin superhydrophilic self-cleaning nanofilm.

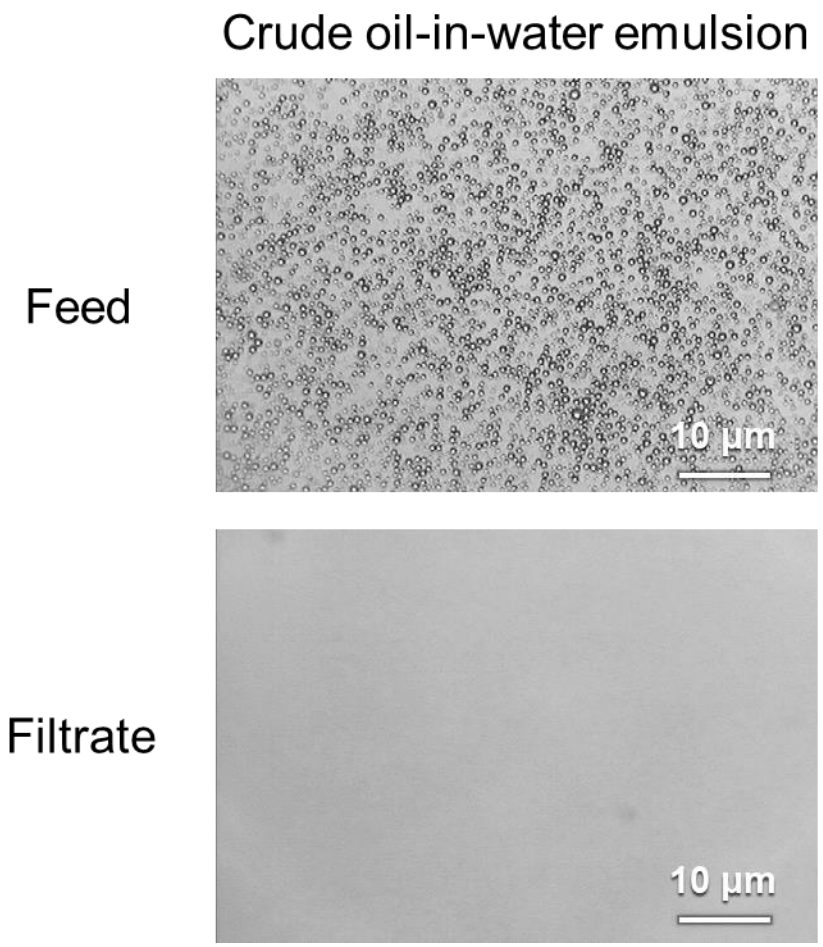

Fig. S15. Optical images of feed and filtrate solutions before and after crude oil-in-water emulsion separation using M-MPN-M.

We captured optical microscope images before and after various emulsion separations using M-MPN-M (**Fig. S15**). There are distinct differences in solutions before and after membrane treatments. The filtrate solutions feature a single phase compared to droplet-scattered biphasic emulsion feeds, indicating valid separation for oil-in-water emulsions.

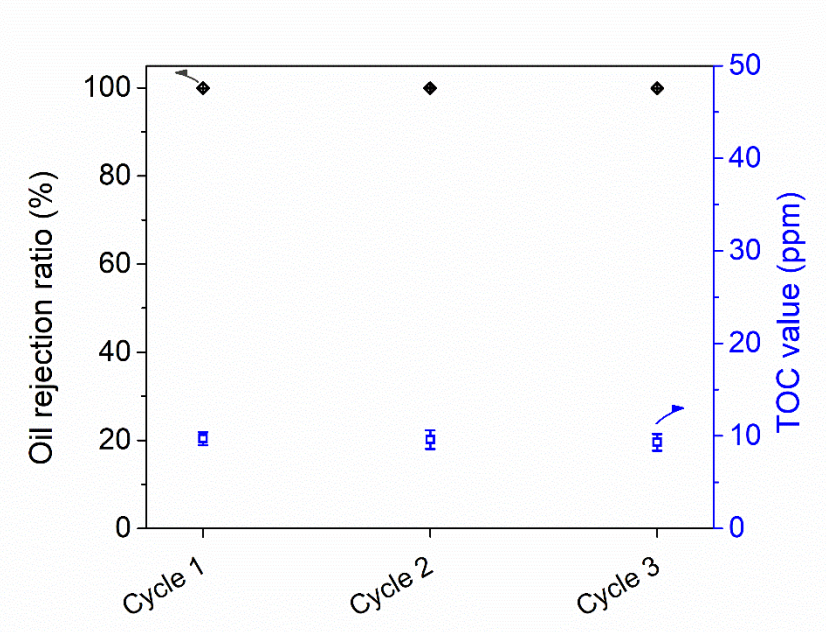

Fig. S16. Oil rejection ratios of M-MPN-M during repeated crude oil-in-water emulsion separations.

Oil rejection was deduced by Equation 9 in the main text when comparing the oil concentration in the feed and permeate solutions using a TOC detector. As shown in **Fig. S16**, the oil rejection ratios surpassed 99.9% with the resultant TOC value below 10 ppm.

Fig. S17. Demonstration of bubble generation of M-MPN-M (arrows point to oxygen bubbles).

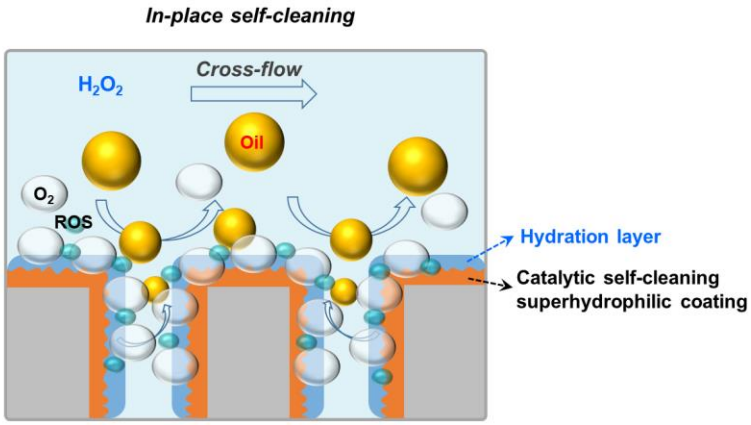

Fig. S18. Synergy of active catalytic antifouling (O_2 bubbles to repel and ROS to degrade) and passive hydration antifouling during M-MPN-M.

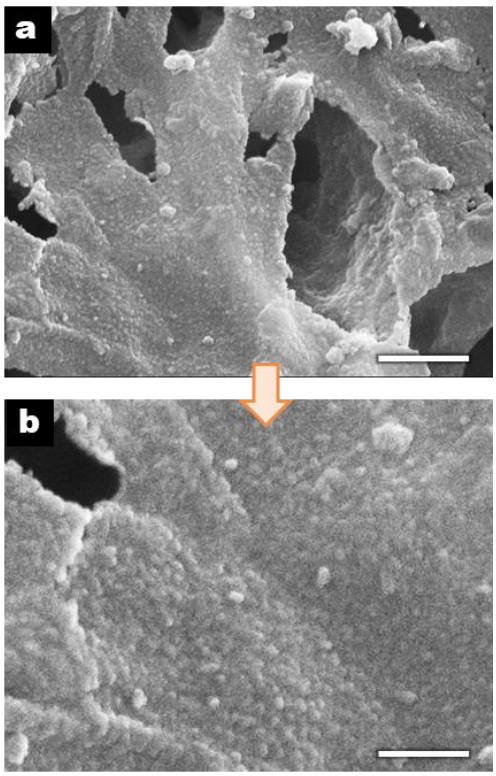

Fig. S19. The SEM image of M-MPN-M after 3-cycles of regeneration with H_2O_2 catalytic cleaning. The scale bar in (a) is 500 nm, in (b) is 200 nm

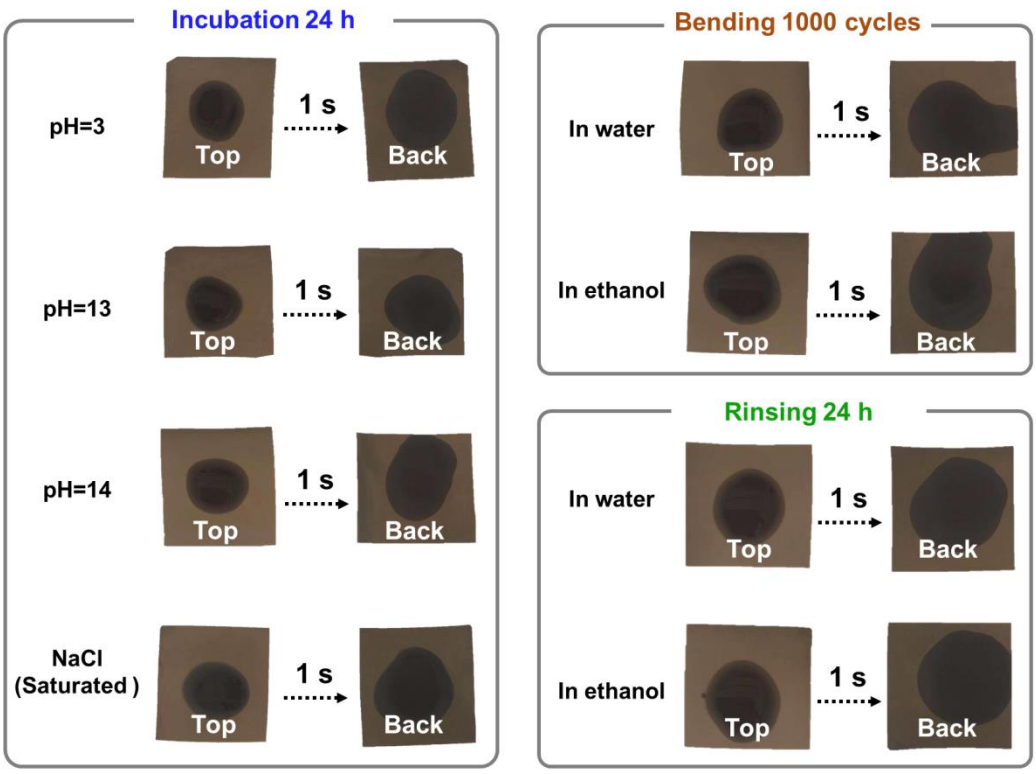

Fig. S20. Water wetting and penetration behaviors of the M-MPN-M membranes with various post-treatments.

As shown in **Fig. S20**, the wetting behaviors of the M-MPN-M samples with various post-treatments, including incubation in acid (pH=3), alkali (pH=13, 14), and saturated NaCl saline, bending in water or ethanol, and rinsing in water or ethanol, were demonstrated. For the incubation treatment, the membrane was placed in a beaker containing testing solutions. Then, the beaker was placed in a shaker, and the rotating speed was set at 80 rpm. For the bending treatment, the operator used two tweezers to clamp two ends of the membrane samples, bent the two ends from the same plane to the parallel state, and then released them to the same plane state and repeated this process until the test cycles. For the rinsing treatment, the membrane was placed on the beaker wall using tape. Then water or ethanol was poured into the beaker until the membrane was totally immersed in the testing liquid. Then, a rinsing test at 3000 r/min proceeded using a magnetic stirrer. The operator should not stick tape on the test region of the membrane during rinsing treatment. As a result, these rigorous treatments had a negligible influence on their water-wetting and penetration behaviors.

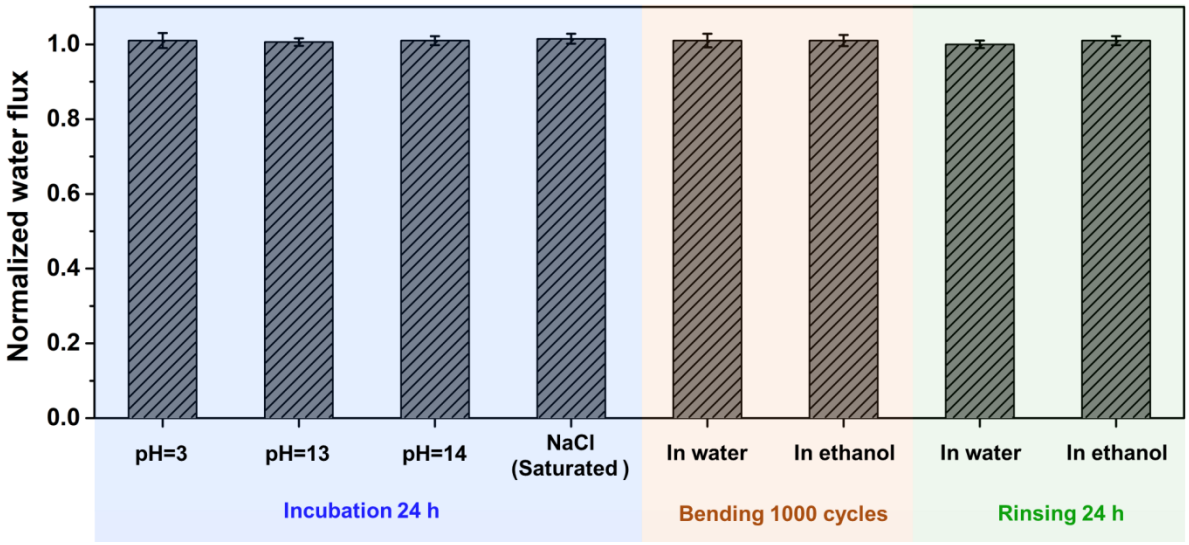

Fig. S21. Normalized pure water permeance of the M-MPN-M membranes with various post-treatments relative to the M-MPN-M membrane without post-treatment.

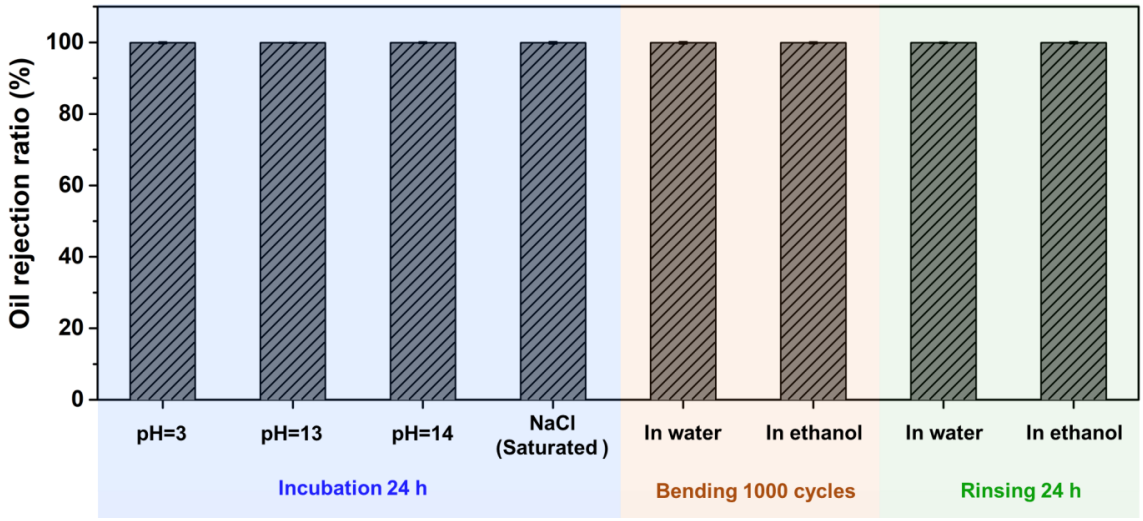

Fig. S22. Oil rejection ratios of the M-MPN-M membranes with various post-treatments.

The stability of the mineralized coating on the membrane surface was tested when considering the complex conditions of practical wastewater. As shown in **Figs. S21 and S22,** M-MPN-M samples with various post-treatments exhibit remarkable stability in pure water permeance and oil rejection ratios. It is beneficial for rigorous demands towards practical complex wastewater treatment.